PHYSICAL SCIENCES

Nonlinear electrohydrodynamic ion transport in graphene nanopores

Xiaowei Jiang[1]†, Chunxiao Zhao[1]†, Yechan Noh[2]†, Yang Xu[1], Yuang Chen[1], Fanfan Chen[1], Laipeng Ma[3], Wencai Ren[3], Narayana R. Aluru[4], Jiandong Feng[1]*

Mechanosensitivity is one of the essential functionalities of biological ion channels. Synthesizing an artificial nanofluidic system to mimic such sensations will not only improve our understanding of these fluidic systems but also inspire applications. In contrast to the electrohydrodynamic ion transport in long nanoslits and nanotubes, coupling hydrodynamical and ion transport at the single-atom thickness remains challenging. Here, we report the pressure-modulated ion conduction in graphene nanopores featuring nonlinear electrohydrodynamic coupling. Increase of ionic conductance, ranging from a few percent to 204.5% induced by the pressure—an effect that was not predicted by the classical linear coupling of molecular streaming to voltage-driven ion transport—was observed experimentally. Computational and theoretical studies reveal that the pressure sensitivity of graphene nanopores arises from the transport of capacitively accumulated ions near the graphene surface. Our findings may help understand the electrohydrodynamic ion transport in nanopores and offer a new ion transport controlling methodology.

INTRODUCTION

In nature, the diversity of biological ion channels arising from tiny differences in atomic arrangements has led to abundant ionic functionalities such as voltage activation, selective transport, and mechanosensitive conduction (*1*). On one hand, ongoing structural analysis of biological channels has provided the basis for biophysical modeling and fundamental insights. On the other hand, the scaling of artificial nanofluidic systems to the molecular scale has revealed a wealth of interesting physics of electrohydrodynamic ion transport (*2*–*4*). As a result, synthetic systems have started to mimic the fundamental roles of their natural counterpart from various aspects (*5*–*7*). However, achieving the performance of natural ion channels such as high selectivity and environmental sensitivity remains challenging.

Recent advances in nanofluidic devices exploiting nanopores, nanotubes, and two-dimensional nanoslits have allowed strong confinement of the transport of ions and water in reduced dimensions (*3*, *8*–*14*), offering unique opportunities for exploring hydrodynamic and correlated ion transport phenomena. Electrohydrodynamic ion flow has been of late observed in confined two-dimensional nanoslits (*3*) and nanotubes (*2*) with channel length in the micrometer scale. In contrast, coupling hydrodynamical and ion transport at the ultimate single-atom length scale remains experimentally unexplored. Nanopores in two-dimensional materials are of particular interest due to the ultrathin transport barrier, exhibiting excellent performance in ion transport (*9*, *15*), energy harvesting (*8*), molecular sieving (*16*, *17*), water transport (*18*), and desalination (*19*, *20*). Theoretical research using computational simulations predicted giant mechanosensitive potassium conductance in graphene crown ethers nanopores (*21*, *22*), highlighting the importance of in-plane strain control over the ion transport in graphene nanopores. The experimental demonstration of mechanosensitive graphene nanopores remains a substantial challenge due to the difficulties of precision nanofabrication and integration of mechanical force. Mechanosensitivity in biological ion channels, MscS or MscL, arises from the response to membrane tension or spring-like tether effect (*23*), while the mechanosensitive ion flow in artificial channels is usually subjected to transmembrane pressure–induced mechanical control (*2*–*4*). Nanopores in two-dimensional materials provide a unique and well-controlled platform to explore such effects, because they exhibit markedly high water flux and pronounced surface effects, such as ion selectivity (*8*) and the emergence of charge anisotropy (*24*). It is therefore essential to know how the molecular level interactions in this atomically thin nanopore system control ion transport, and such an understanding is currently lacking.

RESULTS AND DISCUSSION

In this work, we report the first experimental observation of a pressure-sensitive ion conduction in single graphene nanopores and the mechanism leading to the observed phenomenon. The device configuration is illustrated in Fig. 1 where an individual nanopore in a suspended single-layer graphene membrane connects two fluidic reservoirs filled with aqueous solution of salts (Fig. 1D). A regulated air pressure drop is applied in the same direction of the electric field, thus coupling hydrodynamic ion transport to voltage-driven ion conduction. The graphene nanopore devices were fabricated according to our previously established protocol for MoS_2 nanopores and similar nanopores in two-dimensional materials (Materials and Methods and figs. S1 to S4) (*25*, *26*). We design nanopores in single-layer graphene with a diameter in the range of 1.7 to 16.4 nm. Mechanical stability of graphene membranes is maintained by suspending them on a 20-nm-thick, nanometer-sized silicon nitride hole (60 to 160 nm) that supports the membrane to bear imposed pressures in the range of 0 to 2.5 bar without breaking (Fig. 1 and figs. S5 to S8). To know whether the nanopores are permanently damaged by the pressure or not, repetitive pressure applications are

[1]Laboratory of Experimental Physical Biology, Department of Chemistry, Zhejiang University, Hangzhou 310027, China. [2]Department of Mechanical Science and Engineering, University of Illinois at Urbana-Champaign, Urbana, IL 61801, USA. [3]Shenyang National Laboratory for Materials Science, Institute of Metal Research, Chinese Academy of Sciences, Shenyang 110016, China. [4]Walker Department of Mechanical Engineering, Oden Institute for Computational Engineering and Sciences, The University of Texas at Austin, Austin, Texas, TX 78712, USA.
*Corresponding author. Email: jiandong.feng@zju.edu.cn
†These authors contribute equally to this work.

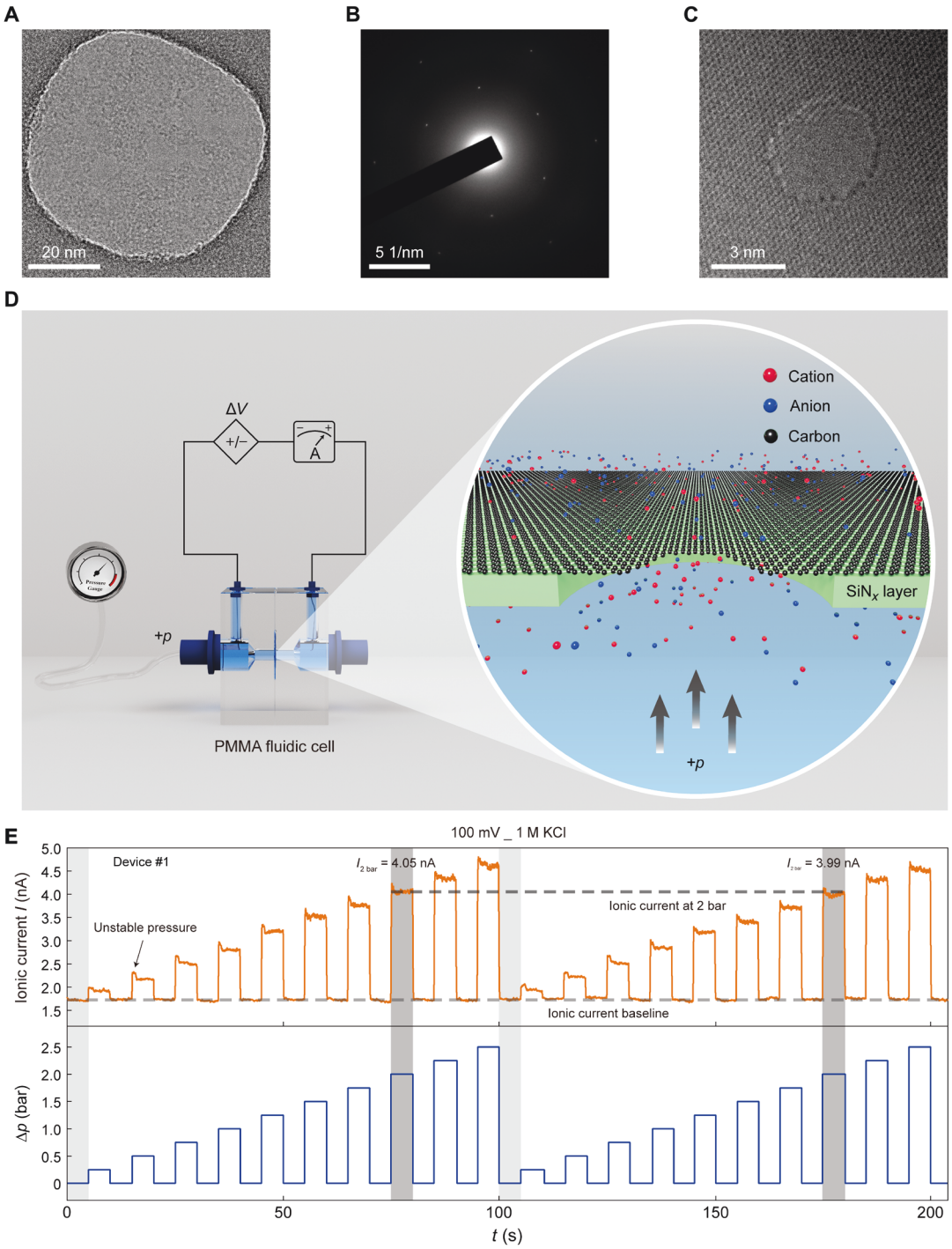

Fig. 1. Graphene nanopores under pressure regulation. (**A**) TEM image of graphene membrane on a 70-nm supporting silicon nitride (SiN_x) hole. (**B**) Electron diffraction pattern of the graphene membrane. (**C**) Aberration-corrected TEM image of a 4-nm graphene nanopore. (**D**) Schematic illustrating the pressure-integrated ion transport in graphene nanopores. The positive direction of applied pressure is indicated in gray arrows. (**E**) Ionic current time trace under a stepwise pressure at 100-mV bias in 1 M KCl solution. The pressure is gradually applied in the range of 0 to 2.5 bar with a step of 0.25 bar for 5-s intervals. Colored regions indicate the current values at 0 and 2 bar. The horizontal dotted lines reveal current levels during repetitive pressure applications. The diameter of the graphene nanopore device #1 is 2.2 nm.

used through all our measurements (figs. S5 and S6). By integrating this regulated pressure drop across the nanopore membrane, we manage to directly couple mechanical force to ion transport, which is then probed by ionic current measurements.

A representative experiment shown in Fig. 1E reveals a strong ionic current response to applied pressure—the increase of ionic current with the sequential buildup of pressures. Remeasuring the same devices by repeating pressure and voltage applications

suggests that the pores are not altered under the measurement conditions, and the observed phenomenon is recoverable in the same devices (Fig. 1E and figs. S5 to S9). Under a fixed bias of 100 mV, the ion current increases from 1.68 to 4.51 nA upon the application of Δp = 2.5-bar pressure difference (Fig. 2A). Figure 2B shows the linear current voltage (I-V) characteristics, and its slope (conductance) increases with increasing applied pressure. For conductance analysis, streaming current and conductance are defined as follows: $I_{str} = I - I_{\Delta p = 0}$ and $G_{str} = I_{str}/\Delta\phi$, respectively, where $\Delta\phi$ is the voltage difference across the membrane. Figure 2C shows a monotonic increase of streaming conductance ratio with pressure, $G_{str}/G_0 \propto \Delta p$ (168.5% increase at 2.5 bar), where G_0 is the conductance without applied pressure, indicating a nonlinear electrohydrodynamic coupling in streaming current, $I_{str} \propto \Delta\phi\Delta p$ (for the same direction of pressure gradient and electric field). The ion current is symmetric with the direction of the pressure gradient (Fig. 2F) following the relation, $I_{str} \propto \Delta\phi\,|\,\Delta p\,|$. Note that this nonlinear streaming current is significantly larger than the typical streaming current and is subject to voltage control. For example, the streaming current in device #1 is about 0.1 nA at 2.5 bar at zero voltage (Fig. 2A). However, under 100 mV, the same pressure generates 2.8 nA (Fig. 2A).

Overall, a similar trend of increase in conductance with pressure has been found for all the devices successfully measured. However, quantitatively, each nanopore device exhibited a markedly different pressure-sensitive response (Fig. 3). For instance, in another device with the same designed pore size (2.4 nm), the ion current and conductance only increased by 2.2% at Δp = 2 bar (Fig. 3F). To gain a better insight into this diverse performance, we investigated a number of possibilities from sample preparation to ionic control to identify its causes. We optimized the transfer process by using a polyvinyl alcohol (PVA)–assisted graphene transfer approach (*27*) to obtain relatively clean samples and then examined the final membrane quality by transmission electron microscopy (TEM) imaging (details and comparison in figs. S2 and S4). We reported a total of 63 nanopore devices (see Figs. 1 to 3 and the Supplementary Materials), which display a dynamic range of response (e.g., 3.7 to 177.9% at Δp = 2 bar in 1 M KCl solution for the 1.7-nm nanopores, as shown in Fig. 3, C and F).

Because of several orders of magnitude difference in pressure-induced mechanical force and electric force governing ion transport as well as the requirement of ion selectivity for the former case, typical values of streaming current in nanofluidic devices are relatively small in comparison to the ion drift–diffusion current (*28*, *29*). The present pressure-sensitive current in graphene nanopore is fundamentally different from the conventional streaming current due to the selective ion transport, which stems from Debye screening of ions within the pressure-induced flow, generally exhibiting linear response to pressure given by the Smoluchowski relation (*30*), $I_{str} \propto \Delta p$. The current observation significantly departs from the classical picture of electrokinetic transport theory (*31*), describing hydrodynamic and ion drift–diffusion transport, as detailed in our numerical model [finite element method (FEM) model in Materials and Methods].

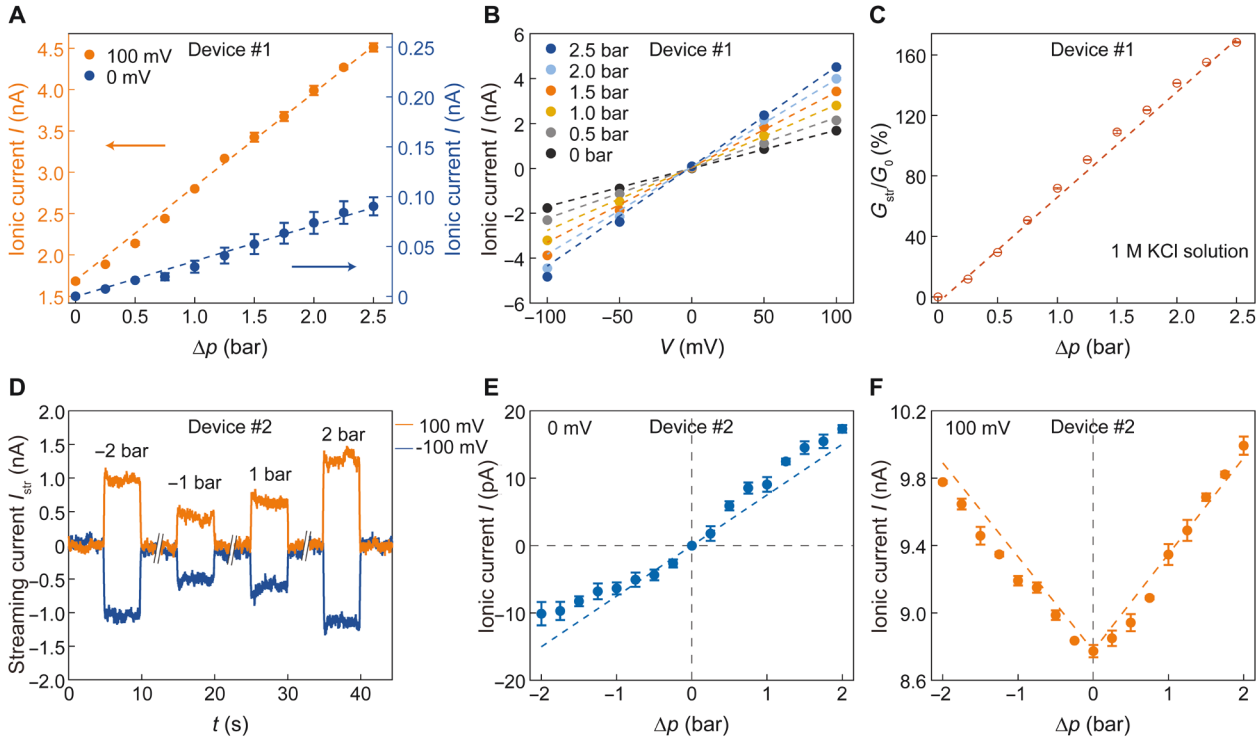

Fig. 2. Mechanosensitive ion transport in graphene nanopores. (**A**) Ionic current as a function of applied pressure at 0 (blue dots, right axis) and 100 mV (orange dots, left axis). (**B**) I-V curves measured as a function of applied pressure. (**C**) Ionic conductance increases as a function of applied pressure. (**D**) Streaming current time trace under different pressures at −100 (blue curve) and 100 mV (orange curve). (**E**) Streaming current as a function of applied pressure at 0 mV. Negative pressure indicates the inverse of pressure direction with respect to the positive direction marked in Fig. 1D. (**F**) Ionic current as a function of applied pressure at 100 mV. The measurements correspond to 1 M KCl solution. The pore sizes of device #1 and device #2 are 2.2 and 8.8 nm, respectively. Error bars are from the error analysis described in Materials and Methods. The dashed lines represent the fit of the theory.

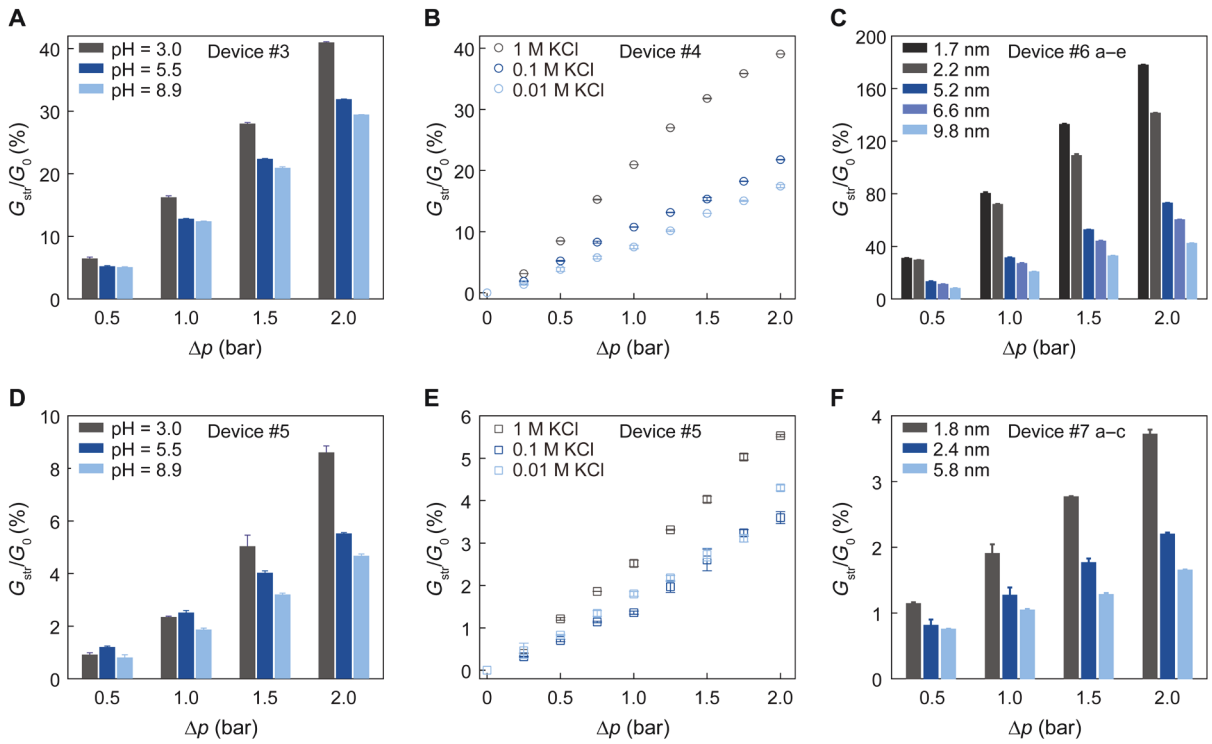

Fig. 3. Mechanosensitive conductance for different ionic environments. (**A**) Mechanosensitive conductance change ratios G_{str}/G_0 under pH control (pH = 3.0, 5.5, and 8.9) for a 7.1-nm graphene nanopore device #3. (**B**) Mechanosensitive conductance change ratios under different ion concentrations (0.01, 0.1, and 1 M KCl) versus pressure for a 7.5-nm graphene nanopore device #4. (**C**) Mechanosensitive conductance change ratios as a function of pore sizes (1.7 to 9.8 nm; device #6, a to e). To make a comparison, the size dependence is performed by enlarging nanopores using electrochemical reaction (ECR) protocol (see details in Materials and Methods). (**D**) Mechanosensitive conductance change ratios under pH control (pH = 3.0, 5.5, and 8.9) for a 7.2-nm graphene nanopore device #5. (**E**) Mechanosensitive conductance change ratios under different ion concentrations (0.01, 0.1, and 1 M KCl) versus pressure for a 7.2-nm graphene nanopore device #5. (**F**) Mechanosensitive conductance change ratios as a function of pore sizes (1.8 to 5.8 nm; device #7, a to c).

Classical streaming current predicts a pressure current depending on the direction of the applied pressure and selective ion transport, which does not explain the current data presented in Fig. 2B.

Several factors influence the pressure-driven ion transport in this system, including the pore geometry, ionic environment, and driving conditions. We systematically compared the influence of ion concentrations, ion types, solution pH, and pore sizes for devices displaying different responses, as shown in Fig. 3, table S1, and figs. S10 to S17. Figure 3 (C and F) shows that the pressure sensitivity increases with decreasing pore size (i.e., with increasing surface-to-volume ratio), which implies relevance to a current through the surface. From detailed conductance-concentration relations, we found a wide distribution of surface charge (12.0 to 26.6 mC/m^2) for graphene nanopores in fig. S18, which may be attributed to the inhomogeneous nature of edge atom arrangement and composition, in agreement with reported range of surface charge (*32*). The observation of the enhanced sensitivity at different concentrations (1 and 0.1 M) and at low pH (3.0) (Fig. 3, A, B, D, and E, and figs. S14 to S16) clearly indicates that the current phenomenon is not the effect of surface charge–governed ion transport (*33*), because graphene nanopore is known to carry weak charges at pH = 3 (*32*). Graphene nanopore tends to have a hydrophobic surface because of the carbon atom–terminated edges and possible polymer residuals. Wetting issues or the presence of nanobubbles in hydrophobic nanopores may lead to irreversible conductance switching between open and close states (*34*, *35*). Our graphene nanopore devices were wetted and treated using various protocols such as solvent wetting (fig. S19) to remove such issues, as evidenced using the criterion of noise spectral analysis shown in fig. S20.

Marked pressure-driven ion transport reported in glass nanocapillaries has been shown to be due to the deformation of spatially charged zones (*4*). However, in that case, the capillaries are unsymmetrical and exhibit rectifying ion transport, which does not account for the current observations. Low friction model of water on long carbon nanotubes developed for capturing quadratic pressure dependence (*2*) may not apply to the ultrathin nanopore case considered here. We discuss how this term can vanish at the ultrathin limit in the "Theory of pressure-sensitive ion transport" section. We also investigated the possibility of the mechanical deformation of graphene membranes by conducting atomic force microscopy indentation experiments (*36*) (figs. S21 to S23) and by performing molecular dynamics (MD) simulations (fig. S24). Nevertheless, all these efforts cannot fully explain the key features of the present experimental findings, and we thus exclude these possibilities (details in the Supplementary Materials).

To gain an insight into the physical mechanism of the pressure sensitivity of the graphene nanopore, we performed MD simulations and successfully reproduced the nonlinear coupling in the pressure-sensitive current found through the experiments $I_{str} \propto \Delta\phi\,|\,\Delta p\,|$ (fig. S25). This pressure-sensitive current amplifies with the voltage

bias and almost vanishes at zero voltage bias, generating only picoampere scale linear streaming current (fig. S25), similar to the experimental results (Fig. 2E). Figure 4F shows the net charge distribution and local current density vectors under a voltage bias without pressure difference. It shows strong net ionic charge layers at the graphene surface, which are created due to a capacitive mechanism and the amount of accumulated ionic charges that are proportional to the dielectric permittivity of the membrane and the bias voltage [see Poisson-Nernst-Planck–Navier-Stokes (PNP-NS) calculation in figs. S26 and S27]. Figure 4G shows that these net charge layers at the membrane surface are transported by mechanical driving forces (i.e., water streaming drags the cation-enriched layer to the cathode side when $\Delta\phi > 0$ and $\Delta p > 0$), creating the nonlinear pressure-voltage coupling. Note that this mechanism explains why the pressure-sensitive current is symmetric about the direction of the pressure gradient (e.g., water streaming drags anion-enriched layer to the anode side when $\Delta\phi > 0$ and $\Delta p < 0$). The hydrodynamic slip is one of the crucial factors in the mechanosensitive current (Fig. 4, H and I), because the pressure-driven flow through a nanopore is closely related to the slip. Thus, the device-to-device variations of pressure sensitivity in graphene nanopore may be understood by the high variation of slip properties on water-carbon interface (*11*, *12*, *14*). Note that our MD simulations (relatively high pressure/voltage used in simulations) only qualitatively conform to the major

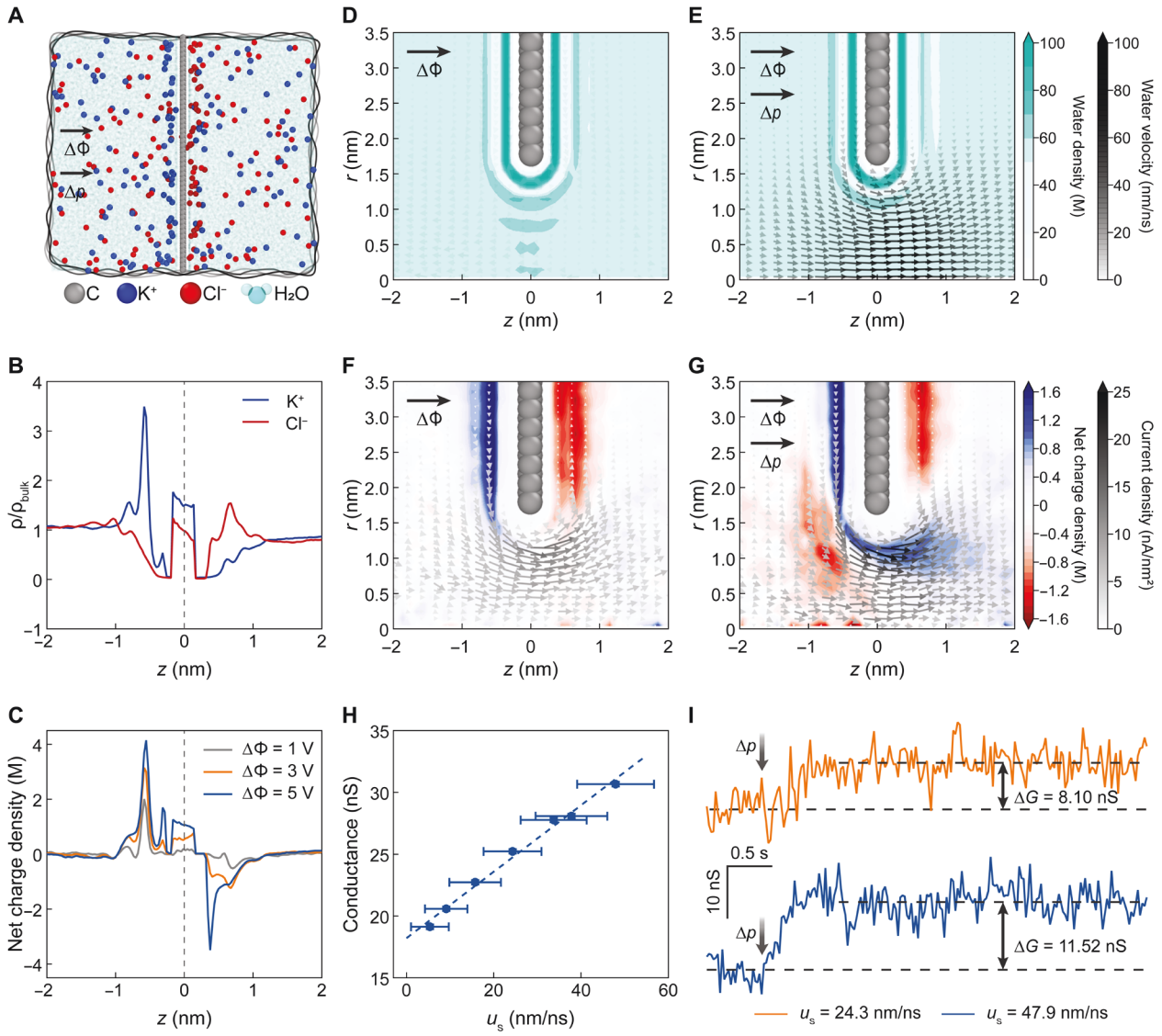

Fig. 4. MD simulation of mechanosensitive ion transport. (**A**) Graphical representation of simulation domain for ion transport through a single-layer graphene nanopore under an electric potential difference and a pressure gradient across the membrane. The accessible diameter of nanopore is 2.6 nm. (**B**) Ion density profile across the membrane under $\Delta\phi = 3$ V and $\Delta p = 200$ MPa. (**C**) Net charge density profile across the membrane under $\Delta p = 200$ MPa. (**D** and **E**) Visualization of axisymmetric water density and velocity vector near the nanopore for (D). $\Delta\phi = 3$ V with zero pressure bias; (E) $\Delta\phi = 3$ V and $\Delta p = 200$ MPa. The large arrow represents the direction of pressure decrease or voltage decrease. (**F** and **G**) Visualization of axisymmetric net charge distribution and current density vectors for (F). $\Delta\phi = 3$ V with zero pressure bias; (G) $\Delta\phi = 3$ V and $\Delta p = 200$ MPa. (**H**) Conductance versus slip velocity. Slip velocity is obtained as the fluid velocity at the first fluidic layer of the pore wall. (**I**) Current over time for different slip velocities.

features of our experimental data due to the limitations of the classical MD approach, which can be potentially improved by optimizing the simulation cell geometry (*37*, *38*) and by implementing more accurate multiscale computational approaches. Our present MD understanding is, however, the foundation for building the later numerical simulations and the theoretical model. In addition, the pressure-sensitive response can be demonstrated by an extended PNP-NS model considering the dielectric permittivity of membrane and the hydrodynamic slip (figs. S26 and S28).

Here, we present a theoretical model for the pressure-sensitive current based on the above physical image (details in Materials and Methods). The streaming current accounting for the physics described above is given by

$$I_{str} = G^{p}_{\varepsilon_m}\Delta\phi + \mu_{eo}\Delta p$$

where $G^{p}_{\varepsilon_m}$ is the mechanosensitive conductance given by $G^{p}_{\varepsilon_m} = \frac{2\varepsilon_m\varepsilon_0\beta^p}{LR}P_Q|\Delta p|$ in units of A/V, ε_m is the dielectric permittivity of the membrane, ε_0 is the vacuum permittivity, β^p is a prefactor, L is the membrane thickness, R is the pore radius, P_Q is the permeation coefficient defined as $P_Q \equiv \frac{Q}{\Delta p}$, and μ_{eo} is the electroosmotic mobility in units of A/Pa. The pressure-sensitive current, $I_{\varepsilon_m,p} = G^{p}_{\varepsilon_m}\Delta\phi \propto |\Delta p|\Delta\phi$, involves the nonlinear coupling between pressure and electric potential. The coupling between pressure and electric potential arises, because the amount of ion accumulation at the membrane is proportional to the voltage and its transport is proportional to the pressure. A detailed derivation and discussion on the theory can be found in Materials and Methods.

The theory fits our experiments, and we see a large range of slip length from 0.4 to 100.8 nm (fig. S29). The divergence of slip length across different devices may originate from the intrinsic graphene surface properties governing the interaction with water and shapes of graphene that are hard to access experimentally in the atomic scale (*12*, *39*–*41*), for example, the number of dangling bonds and disordered graphene pore edge, which may require more accurate theory such as ab initio MD and better experimental approaches to probe. In addition to device-to-device heterogeneities, the slip length of the same nanopore device can be still affected by the surface charge, the solvent, and ion absorption at the interface. On the basis of our theory, we could experimentally address the slippage contribution under zero bias to avoid its coupling with electrokinetically driven capacitive ion accumulation. Figure S30 supports that the large variation of slip is the major contribution to the current observation, as the marked difference of streaming current is already observed at zero bias for devices displaying different pressure sensitivities. Precise bottom-up assembly of graphene pore chemistry might be a promising way to yield uniform nanopore devices in future, which may potentially address the issue of the performance divergence (*5*). In addition to slip, our theory and simulation (fig. S26) suggest the dielectric modulation of graphene membrane as an alternative approach to control this pressure-sensitive effect. To identify the possibility of tuning the response, we further designed various types of substrates for suspending the graphene membranes, graphene nanopores with different thickness, and single-layer MoS_2 nanopores for the pressure-modulated experiments. As discussed in figs. S31 to S33, the dielectric tuning, thickness, and pore material–varying results suggest the feasibility of this strategy in regulating the pressure-induced ion transport modulation.

To summarize, we have experimentally explored the first pressure-sensitive ion transport phenomenon using ultimate thin barriers in individual graphene nanopores. This pressure modulation of ion conduction involves nonlinear electrohydrodynamic coupling, which cannot be predicted by the classical picture of the linear electrokinetic theory. We performed extensive experiments under various conditions and consistently observed the nonlinear modulation in single-layer graphene nanopores. Our MD simulation revealed that this phenomenon arises from the strong capacitive accumulation of ions at each side of the graphene membrane under the voltage- and pressure-driven transport. Our work thus opens a new dimension for achieving efficient pressure sensitivity toward active control of ion transport at the nanoscale and developing advanced biomimetic ionic devices.

MATERIALS AND METHODS

Graphene membrane transfer

High-quality chemical vapor deposition–grown graphene membranes were prepared using the method reported by Gao *et al.* (*42*). Before graphene transfer, the 20-nm-thick silicon nitride (SiN_x) membranes were manufactured in a previously reported procedure (*26*) using lithography and anisotropic KOH wet etching (membrane sizes ranged from 10 × 10 to 25 × 25 μm^2) or supplied from NORCADA Chips (membrane size: 12 × 12 μm^2; 60- to 70-nm supporting hole). Focused ion beam (FIB) was applied to make 60- to 300-nm supporting holes on the membrane. Single-layer graphene was transferred to the SiN_x membrane using three transfer methods as illustrated in fig. S1. The polymethylmethacrylate (PMMA) transfer method (*43*) relies on the use of PMMA [weight-average molecular weight (M_w) = 950 kg/mol] film to support the graphene membranes and to prevent them from folding during the etching of the copper foil. The millimeter-scale graphene membranes on a copper foil were coated by PMMA and floated in 0.1 M ammonium persulfate [$(NH_4)_2S_2O_8$] solution (*44*). After all the copper layers were etched away, the graphene membrane with the PMMA film was transferred to a FIB opening located on the SiN_x membrane. The PMMA layers were then removed by acetone. The devices were further annealed at 500°C for 3 hours under the flowing protecting gas argon (100 standard cubic centimeter per minute) to remove the PMMA residual left on the surfaces. The difference of PVA-assisted transfer method (*27*) is that a PVA film is inserted between the PMMA layer and the graphene membrane. A total of 150 mg of PVA and 20 ml of deionized water were put in a small beaker, and then the PVA solution is heated and stirred on a 120°C heating plate for 2 hours. The cooled solution was used for spin coating before using PMMA. The PMMA residues were removed by dissolving the PVA films in acetone at 50°C and deionized water at 100°C. The tape method used a thermal release tape (Graphene Market) instead of PMMA as graphene support. The tapes were detached from the graphene membranes at 100°C.

Nanopore fabrication

The graphene nanopores were fabricated using either the previously reported atomic scale–controlled ECR technique (*25*) or TEM-based electron irradiation (*26*). ECR was done by applying a step-like transmembrane voltage and monitoring the transmembrane current using a low-noise current amplifier (FEMTO Messtechnik GmbH). The critical voltage was shut down immediately by a custom-made

feedback control program once the desirable pore conductance/size was reached. We estimated the pore size based on the conductance measurements in 1 M KCl solution using an analytical model (*25*, *32*), described by

$$G = \sigma \left[\frac{4L}{\pi d^2} + \frac{1}{d} \right]^{-1} \quad (1)$$

where G, σ, L, and d are the pore conductance, solution conductivity (10.8 S m^{-1}), effective thickness of the graphene membrane [0.6 nm (*45*)], and nanopore diameter, respectively.

For calibration, graphene nanopores were drilled by focusing the electron beam using a JEOL 2100F high-resolution transmission electron microscope operated at 200 kV. A customized sample holder was used to place the squared SiN_x chip that graphene was transferred on. Once an appropriate graphene nanopore was formed, the focused electron beam was scattered quickly and followed by taking TEM images. The operation must be conducted as fast as possible to avoid the additional damage of the electron beam on the sample. Aberration-corrected TEM imaging was acquired using a FEI Titan G2 60-300 TEM operated at 80 kV.

Pressure-sensitive ion transport measurements

The chip with formed one graphene nanopore was mounted in the custom-made PMMA chambers (see Fig. 1) as described before (*25*). After mounting, the nanopore was wetted with degassed water:ethanol (v/v, 1:1) solution for at least 45 min to remove bubbles trapped in the chambers. After changing to the degassed salt solutions (various ion types, ionic concentrations, and pH values; Sigma-Aldrich), two PMMA chambers on both sides of the chip were sealed by threaded tee joints containing a pair of chlorinated Ag/AgCl electrode, and a gas pipe was connected to a voltage-controlled pressure regulator (SMC Corp.). The regulator used to apply pressure was connected to an air compressor via filters (SMC Corp.). A pair of Ag/AgCl electrode was used to apply the voltage, and the current between the two electrodes was detected using an Axopatch 200B patch-clamp amplifier (Molecular Devices). We used a NI PXI-4461 card for data digitalization. The ionic current was recorded by applying a step-like pressure sweep (varying typically from 0 to 2.5 bar in 0.25-bar steps for 5-s intervals) that was executed at least 3 cycles at a constant voltage bias (ranging typically from −100 to 100 mV with a step of 50 mV), and then we analyze the SD of current time trace as the error bars of the data from three experimental repetitions. The typical current time trace was shown in figs. S5 and S6.

The ionic conductance under different applied pressures was obtained by fitting the I-V data. We defined the streaming conductance change ratio, G_{str}/G_0, as the increased conductance with applied pressure divided by the conductance without applied pressure to determine the pressure-sensitive response.

MD simulations

All-atom MD simulations are conducted to elucidate the physical origin of the pressure-sensitive ion transport observed in a single layer of graphene nanopore. The system contains two electrolyte reservoirs (12 nm × 12 nm × 7 nm each) separated by a single layer of graphene nanopore with an accessible diameter of 2.6 nm. The reservoirs contain 1 M KCl aqueous solution. The fluid-fluid and fluid-solid interactions are modeled as Lennard-Jones (LJ) potential with a cutoff distance of 12 Å. The SPC/E model (*46*) is used for water molecules. For carbon-carbon interactions, Tersoff potential optimized for lattice dynamics of graphene (*47*) is used. Ion-water force fields are adopted from Joung *et al.* (*48*), and graphene-water force field is taken from Wu and Aluru (*49*). Lorentz-Berthelot mixing rule is used for the rest of atomic pairs. In the case study for various slips, we modified the depths of the LJ potential well between the fluid molecules (water and ions) and carbon atom from $0.1\epsilon_{fluid-carbon}$ to $10.0\epsilon_{fluid-carbon}$. Partial charges of graphene are uniformly distributed to correspond to its charge density (σ = 0 or 18 mC/m^2). The dipole polarizability of carbon is not considered; thus, the dielectric permittivity of graphene is equal to vacuum permittivity, $\varepsilon_m = 1$. For pressure-sensitive ion transport, a constant electric field (*50*) is applied. The system is equilibrated at room temperature in NVT ensemble for 1 ns with a 1-fs time step. The thermostat only adjusts x and y velocity components to minimize the disturbance on the ion transport. A constant force corresponding to (50 to 300 MPa) is applied to the fluid molecules in the edge of the reservoir (1-nm-thick box). The applied force is calculated using $\frac{nF}{A} = P$, where n is the number of the fluid molecules (water and ions) in the force applied region, F is the force applied, A is the cross-sectional area of the system perpendicular to the applied force, and P is the corresponding pressure. The ion current is directly measured by counting the number of passing ions over time. The SHAKE algorithm is used to constrain bond angles and lengths of SPC/E water (*51*). The Particle–particle–particle–mesh method is used to calculate electrostatic potential. To expedite MD simulation, GPU-accelerated computation is used (*52*). The Large-scale Atomic/Molecular Massively Parallel Simulator (*53*) is used for all MD simulations, and Open Visualization Tool OVITO (*47*) is used for visualization.

PNP-NS model

For pressure-sensitive ion transport, the dielectric permittivity of membrane and hydrodynamic slip at the membrane surface need to be considered in PNP-NS calculation. COMSOL Multiphysics 5.5 is used for the FEM calculation. The ion fluxes are described by the Nernst-Planck equation

$$\mathbf{J}_i = -D_i \nabla \rho_i - \frac{z_i e}{k_B T} D_i \rho_i \nabla \phi + \rho_i \mathbf{u} \quad (2)$$

where $\mathbf{J}_i$ is the ion flux vector, D_i is the diffusion coefficient, ρ_i is the density of ion in unit m^{-3}, z_i is the charge number, i in the subscript indicates charge species ($i = K^+$ or Cl^-), e is the elementary charge, k_B is the Boltzmann constant, T is the temperature, ϕ is the electric potential, and $\mathbf{u}$ is the fluid velocity. The Poisson equation gives the relationship between the electric potential ϕ and ion concentration c_i

$$\nabla^2 \phi = -\frac{F}{\varepsilon_r \varepsilon_0} \sum_i z_i c_i \quad (3)$$

where ε_r and ε_0 are the relative permittivity of the solution and the vacuum permittivity, respectively. The hydrodynamic flow is described by the Navier-Stokes equation (*54*) for an incompressible fluid in a steady state

$$\rho_w(\mathbf{u}\nabla\mathbf{u}) = -\nabla p + \eta \nabla^2 \mathbf{u} - e \sum_i z_i c_i \nabla \phi \quad (4)$$

where ρ_w, η, and p are the water density, viscosity, and pressure, respectively.

The geometry of the model used a two-dimensional axisymmetric system and is shown in fig. S24A. A single-layer graphene with a thickness of 0.34 nm is considered with permittivity ε_m in region 3. In this solid region, only the Poison equation is solved. In region 2, one layer of water molecules (thickness of 0.34 nm) is considered. In this water layer, the Poisson equation and the Navier-Stokes equation are solved with the slip boundary condition (*55*). For the electrolyte in region 3, all PNP-NS equations are solved. At each side of reservoir, a constant electric potential difference, $\Delta\phi$, and pressure difference, Δp, are set to be the boundary conditions. The reservoir ion concentration is fixed to 1 M and the pore size is set to 1.5 nm. The dielectric permittivity of water is set to be 80 and that of graphene is 3. Diffusion coefficients of cations and anions are set to be 1.45×10^{-9} and 1.51×10^{-9} m^2/s, respectively.

Figure S26B shows how the electric permittivity of membrane affects the concentration profiles for various applied voltages. Figure S26C shows the amount of net ionic charge accumulated on one side of the membrane obtained from PNP-NS and predicted by the parallel plate capacitor model. The pressure-sensitive behavior observed in PNP-NS calculation is shown in fig. S28. The I-V characteristics in the low voltage regime ($\Delta\phi \leq 100$ mV) show linear behavior (fig. S28A) and enhanced by the applied pressure. At high voltage, nonlinear I-V curves are observed (fig. S28B), and this is due to the electrically driven net charges accumulated on the membrane surface (theoretical discussion of this current term is shown in Section Theory of pressure-sensitive ion transport). The current enhancement due to the applied pressure exhibits symmetric V-shaped curves for noncharged membrane (fig. S28C) and slightly tilted (counterclockwise) V-shaped curves for negatively charged membrane (fig. S28D). Thus, the slightly tilted V-shaped curve (counterclockwise) in experiment (Fig. 2F) implies that the graphene used in the experiment has a negative surface charge.

Theory of pressure-sensitive ion transport

We present a simple ion transport theory that consider the effect of dielectric permittivity of membrane involving a nonlinear electrohydrodynamic coupling in the streaming current, $I_{str} \sim \Delta\phi\,|\,\Delta p\,|$. Considering an electrolyte-membrane-electrolyte system under a voltage and pressure difference between the two electrolyte reservoirs (fig. S27), the accumulated net charge at the membrane surface can be obtained by the parallel plate capacitor model

$$q_{\varepsilon_m} = \frac{\varepsilon_m \varepsilon_0 A_m}{L} |\,\Delta\phi\,| \tag{5}$$

where ε_m is the relative permittivity of the membrane, ε_0 is the vacuum permittivity, A_m is the membrane area, L is the membrane thickness, and $\Delta\phi$ is the electric potential difference between the reservoirs, $\phi_1 - \phi_2 = \Delta\phi$. Equation 5, which is typically used in metal-membrane-metal system, is compared with the results of PNP-NS calculation and shows good match especially in high concentration (fig. S26C). Note that the capacitance, $C = \frac{\varepsilon_m \varepsilon_0 A_m}{L}$, is inversely proportional to the thickness of the membrane. Thus, nanofluidic devices with a nanopore in a single layer of graphene membrane (ultrathin membrane) have a high capacitance, although its dielectric permittivity is not high ($\varepsilon_m \sim 3$) (*56*) under a static electric field. The accumulated net charge is assumed to be in an atomically thin ionic layer. This assumption is reasonable for high concentration systems where the Debye length, λ_D, is atomically small (e.g., $\lambda_D \approx 0.3$ nm for 1 M KCl aqueous solution; see the charge distribution from PNP-NS in fig. S26B). For 1:1 electrolyte, the density of accumulated ions (in unit meter^{-2}) at the membrane surface is given by

$$\sigma_\varepsilon = \frac{\varepsilon_m \varepsilon_0}{eL} |\,\Delta\phi\,| \tag{6}$$

where e is the elementary charge. Note that the net charge density at the anode side of the membrane surface ($e\sigma_\varepsilon$) and cathode side of the membrane surface ($-e\sigma_\varepsilon$) have an opposite charge with the same amount, maintaining electroneutrality in the system. These accumulated ions leak to the pore region and increase the overall ion density in the pore generating an additional current. In this modeling, the additional charge carriers are treated as a perturbation of density, $\delta\rho^{\pm}_{\varepsilon_m}(r)$. Consider the classical description of current density, i, under pressure and electric potential difference

$$i(r) = e\{\rho^+(r) + \rho^-(r)\}\mu E_x + e\{\rho^+(r) - \rho^-(r)\}u(r) \tag{7}$$

where the plus and minus superscripts indicate the cation and anion, respectively, $\rho^{\pm}$ is the charge density of ion in unit meter^{-3}, μ is the mobility of ion (assumed to be the same for cation and anion), E_x is the axial electric field, and u is the convective velocity. Considering the perturbation of density due to the membrane permittivity, the total density in the pore is written as $\rho^{\pm}(r) = \rho^{\pm}_{\varepsilon_m=0}(r) + \delta\rho^{\pm}_{\varepsilon_m}(r)$, where $\rho^{\pm}_{\varepsilon_m=0}(r)$ is a classical charge density in the pore without considering membrane permittivity. From the Boltzmann statistics, $\rho^{\pm}_{\varepsilon_m=0}(r) = \rho_0 \exp\left\{\mp \frac{e\psi(r)}{k_B T}\right\}$, where ρ_0 is the ion density in the reservoir and ψ is the pore potential. Then, the current density is written as

$$\begin{aligned} i(r) &= e\{2\rho_0 \cosh\bar{\psi} + \delta\rho^+_{\varepsilon_m}(r) + \delta\rho^-_{\varepsilon_m}(r)\}\mu E_x(r) \\ &+ e\{-2\rho_0 \sinh\bar{\psi} + \delta\rho^+_{\varepsilon_m}(r) - \delta\rho^-_{\varepsilon_m}(r)\}u(r) \end{aligned} \tag{8}$$

where $\bar{\psi}$ is the normalized pore potential given by $\bar{\psi} = \frac{e\psi}{k_B T}$. We introduce the mean field approximation: $\delta\rho^{\pm}_{\varepsilon_m}(r) \approx \delta\,\overline{\rho}^{\pm}_{\varepsilon_m} \equiv \frac{\int_0^R \delta\rho^{\pm}_{\varepsilon_m}(r)\,\mathrm{rdr}}{\int_0^R \mathrm{rdr}}$, $\bar{\psi}(r) \approx \bar{\psi} \equiv \frac{\int_0^R \bar{\psi}(r)\,\mathrm{rdr}}{\int_0^R \mathrm{rdr}}$, and $E_x(r) \approx \frac{\Delta\phi}{L + \alpha R}$, where R is the radius of pore and α is a geometrical prefactor representing the electrical access resistance [e.g., $\alpha = \frac{\pi}{2}$ in the case of Maxwell-Hall access resistance (*57*) for an electrically insulated membrane $\varepsilon_m = 0$]. Ion current, $I = \int_0^R i(r)\,2\pi r dr$, is obtained as

$$\begin{aligned} i(r) &= e\{2\rho_0 \cosh\bar{\psi} + \delta\,\overline{\rho}^+_{\varepsilon_m} + \delta\,\overline{\rho}^-_{\varepsilon_m}\}\mu \frac{\pi R^2}{L + \alpha R}\Delta\phi \\ &+ e\{-2\rho_0 \sinh\bar{\psi} + \delta\,\overline{\rho}^+_{\varepsilon_m} - \delta\,\overline{\rho}^-_{\varepsilon_m}\}Q \end{aligned} \tag{9}$$

where Q is the hydrodynamic volumetric flow rate. Equation 9 consists of three components $I = I^\phi + I^p + I_{\varepsilon m}$, where $I^\phi = G^\phi \Delta\phi$ is the classical electrically driven current with electrical conductance $G^\phi = 2e\mu\rho_0 \cosh\bar{\psi} \frac{\pi R^2}{L + \alpha R}$ (*58*) (in unit A/V), $I^p = \mu_{eo}\Delta p$ is the classical streaming current with electroosmotic mobility $\mu_{eo} = 2e\rho_0 \sinh\bar{\psi} P_Q$ (in unit A/Pa), $P_Q \equiv \frac{Q}{\Delta p}$ is the permeation coefficient, and $I_{\varepsilon m}$ is the additional current due to the dielectric permittivity given by

$$I_{\varepsilon_m} = e(\delta\,\overline{\rho}^+_{\varepsilon_m} + \delta\,\overline{\rho}^-_{\varepsilon_m})\,\mu \frac{\pi R^2}{L + \alpha R}\Delta\phi + e(\delta\,\overline{\rho}^+_{\varepsilon_m} - \delta\,\overline{\rho}^-_{\varepsilon_m})\,P_Q \Delta p \tag{10}$$

The charge leakage from membrane to the pore is proportional to $\sigma_{\varepsilon m}$. The perturbation of density can be written as $\delta\,\overline{\rho}^+_{\varepsilon_m} + \delta\,\overline{\rho}^-_{\varepsilon_m} = \beta^\phi \frac{2\sigma_{\varepsilon_m}}{R}$,

where β^{ϕ} is a prefactor. Similarly, $|\delta\overline{\rho}^{+}_{\varepsilon_m} - \delta\overline{\rho}^{-}_{\varepsilon_m}| = \beta^{p}\frac{2\sigma_{\varepsilon_m}}{R}$, where β^{p} is a prefactor. Note that the sign of $\delta\overline{\rho}^{+}_{\varepsilon_m} - \delta\overline{\rho}^{-}_{\varepsilon_m}$ depends on the direction of pressure and voltage gradient. For example, when the direction of pressure and electric potential gradient are the same (i.e., $\Delta p\Delta\phi \geq 0$), the net charge in the pore is positive. On the other hand, net charge in the pore is negative if the direction of pressure and electric potential gradient are opposite (i.e., $\Delta p\Delta\phi < 0$). The additional current due to the membrane permittivity is obtained as

$$I_{\varepsilon_m} = (G^{\phi}_{\varepsilon_m} + G^{p}_{\varepsilon_m})\Delta\phi \tag{11}$$

where $G^{\phi}_{\varepsilon_m} = 2\pi R\frac{\varepsilon_m\varepsilon_0\beta^{\phi}\mu}{L(L+\alpha R)}|\Delta\phi|$ and $G^{p}_{\varepsilon_m} = \frac{2\varepsilon_m\varepsilon_0\beta^{p}}{LR}P_Q|\Delta p|$. Here, the second term is the pressure-sensitive current where $I^{p}_{\varepsilon_m} = G^{p}_{\varepsilon_m}\Delta\phi \propto |\Delta p|\Delta\phi$. In addition, Equation 11 predicts a nonlinear current component, $I^{\phi}_{\varepsilon_m} = G^{\phi}_{\varepsilon_m}\Delta\phi \propto |\Delta\phi|\Delta\phi$. At low voltage regime, this current component is insignificant ($G^{\phi}_{\varepsilon_m} \sim 0$) compared to the classical current. However, this quadratic term becomes important in a high voltage regime (fig. S28, A and B). Last, the total current can be obtained as

$$I = \{G^{\phi} + G^{\phi}_{\varepsilon_m} + G^{p}_{\varepsilon_m}\}\Delta\phi + \mu_{eo}\Delta p \tag{12}$$

One may include the Péclet number–dependent conductance suggested by Marcotte *et al.* (*2*) where the interplay between the electrical and hydrodynamical driving force leads to the Péclet number–dependent conductance, $G^{\phi}(\mathrm{Pe}) = G^{\phi}\frac{\mathrm{Pe}/2}{\tanh(\mathrm{Pe}/2)}$. The Péclet number is given by $\mathrm{Pe} = \frac{QL}{\pi R^2 D}$, where D is the diffusion coefficient. Then, Eq. 6 can be rewritten as

$$I = \{G^{\phi}(\mathrm{Pe}) + G^{\phi}_{\varepsilon_m} + G^{p}_{\varepsilon_m}\}\Delta\phi + \mu_{eo}\Delta p \tag{13}$$

This is a general form of ion current through a nanopore/tube under a simultaneously applied pressure and voltage difference. Note that, if the membrane is electrically insulated (e.g., thick membrane: $L \gg \frac{\varepsilon_m\varepsilon_0|\Delta\phi|}{Re\rho_0}$ or negligible dielectric permittivity: $\varepsilon_m \ll \frac{LRe\rho_0}{\varepsilon_0|\Delta\phi|}$), then Eq. 13 reduces to the Marcotte *et al.*'s (*2*) theory of pressure-sensitive current: $I = G^{\phi}(\mathrm{Pe})\Delta\phi + G^{p}\Delta p$. On the other hand, in ultrathin membrane (e.g., single-layer graphene nanopore), the Péclet number dependency vanishes due to its negligible thickness, and Eq. 13 reduces to Eq. 12. In this thin limit, the streaming current, $I_{str} \equiv I - I_{\Delta p=0}$, is obtained as

$$I_{str} = G^{p}_{\varepsilon_m}\Delta\phi + \mu_{eo}\Delta p \tag{14}$$

The first term is the pressure-sensitive current due to the membrane permittivity, and the second term is the classical streaming current associated with selective ion transport.

SUPPLEMENTARY MATERIALS

Supplementary material for this article is available at https://science.org/doi/10.1126/sciadv.abj2510

REFERENCES AND NOTES

1. S.-H. Chung, O. S. Anderson, V. V. Krishnamurthy, *Biological Membrane Ion Channels: Dynamics, Structure, and Applications* (Springer Science & Business Media, 2007).
2. A. Marcotte, T. Mouterde, A. Niguès, A. Siria, L. Bocquet, Mechanically activated ionic transport across single-digit carbon nanotubes. *Nat. Mater.* **19**, 1057–1061 (2020).
3. T. Mouterde, A. Keerthi, A. R. Poggioli, S. A. Dar, A. Siria, A. K. Geim, L. Bocquet, B. Radha, Molecular streaming and its voltage control in ångström-scale channels. *Nature* **567**, 87–90 (2019).
4. L. Jubin, A. Poggioli, A. Siria, L. Bocquet, Dramatic pressure-sensitive ion conduction in conical nanopores. *Proc. Natl. Acad. Sci. U.S.A.* **115**, 4063–4068 (2018).
5. L. Bocquet, Nanofluidics coming of age. *Nat. Mater.* **19**, 254–256 (2020).
6. L. Wang, M. S. H. Boutilier, P. R. Kidambi, D. Jang, N. G. Hadjiconstantinou, R. Karnik, Fundamental transport mechanisms, fabrication and potential applications of nanoporous atomically thin membranes. *Nat. Nanotechnol.* **12**, 509–522 (2017).
7. S. Faucher, N. Aluru, M. Z. Bazant, D. Blankschtein, A. H. Brozena, J. Cumings, J. Pedro de Souza, M. Elimelech, R. Epsztein, J. T. Fourkas, A. G. Rajan, H. J. Kulik, A. Levy, A. Majumdar, C. Martin, M. McEldrew, R. P. Misra, A. Noy, T. A. Pham, M. Reed, E. Schwegler, Z. Siwy, Y. Wang, M. Strano, Critical knowledge gaps in mass transport through single-digit nanopores: A review and perspective. *J. Phys. Chem. C* **123**, 21309–21326 (2019).
8. J. Feng, M. Graf, K. Liu, D. Ovchinnikov, D. Dumcenco, M. Heiranian, V. Nandigana, N. R. Aluru, A. Kis, A. Radenovic, Single-layer MoS_2 nanopores as nanopower generators. *Nature* **536**, 197–200 (2016).
9. J. Feng, K. Liu, M. Graf, D. Dumcenco, A. Kis, M. Di Ventra, A. Radenovic, Observation of ionic Coulomb blockade in nanopores. *Nat. Mater.* **15**, 850–855 (2016).
10. A. Siria, P. Poncharal, A.-L. Biance, R. Fulcrand, X. Blase, S. T. Purcell, L. Bocquet, Giant osmotic energy conversion measured in a single transmembrane boron nitride nanotube. *Nature* **494**, 455–458 (2013).
11. E. Secchi, S. Marbach, A. Niguès, D. Stein, A. Siria, L. Bocquet, Massive radius-dependent flow slippage in carbon nanotubes. *Nature* **537**, 210–213 (2016).
12. Q. Xie, M. A. Alibakhshi, S. Jiao, Z. Xu, M. Hempel, J. Kong, H. G. Park, C. Duan, Fast water transport in graphene nanofluidic channels. *Nat. Nanotechnol.* **13**, 238–245 (2018).
13. R. H. Tunuguntla, R. Y. Henley, Y.-C. Yao, T. A. Pham, M. Wanunu, A. Noy, Enhanced water permeability and tunable ion selectivity in subnanometer carbon nanotube porins. *Science* **357**, 792–796 (2017).
14. J. K. Holt, H. G. Park, Y. Wang, M. Stadermann, A. B. Artyukhin, C. P. Grigoropoulos, A. Noy, O. Bakajin, Fast mass transport through sub-2-nanometer carbon nanotubes. *Science* **312**, 1034–1037 (2006).
15. T. Jain, B. C. Rasera, R. J. S. Guerrero, M. S. H. Boutilier, S. C. O'Hern, J.-C. Idrobo, R. Karnik, Heterogeneous sub-continuum ionic transport in statistically isolated graphene nanopores. *Nat. Nanotechnol.* **10**, 1053–1057 (2015).
16. S. P. Koenig, L. Wang, J. Pellegrino, J. S. Bunch, Selective molecular sieving through porous graphene. *Nat. Nanotechnol.* **7**, 728–732 (2012).
17. L. Wang, L. W. Drahushuk, L. Cantley, S. P. Koenig, X. Liu, J. Pellegrino, M. S. Strano, J. Scott Bunch, Molecular valves for controlling gas phase transport made from discrete ångström-sized pores in graphene. *Nat. Nanotechnol.* **10**, 785–790 (2015).
18. K. G. Zhou, K. S. Vasu, C. T. Cherian, M. Neek-Amal, J. C. Zhang, H. Ghorbanfekr-Kalashami, K. Huang, O. P. Marshall, V. G. Kravets, J. Abraham, Y. Su, A. N. Grigorenko, A. Pratt, A. K. Geim, F. M. Peeters, K. S. Novoselov, R. R. Nair, Electrically controlled water permeation through graphene oxide membranes. *Nature* **559**, 236–240 (2018).
19. S. P. Surwade, S. N. Smirnov, I. V. Vlassiouk, R. R. Unocic, G. M. Veith, S. Dai, S. M. Mahurin, Water desalination using nanoporous single-layer graphene. *Nat. Nanotechnol.* **10**, 459–464 (2015).
20. Y. Yang, X. Yang, L. Liang, Y. Gao, H. Cheng, X. Li, M. Zou, R. Ma, Q. Yuan, X. Duan, Large-area graphene-nanomesh/carbon-nanotube hybrid membranes for ionic and molecular nanofiltration. *Science* **364**, 1057–1062 (2019).
21. A. Fang, K. Kroenlein, D. Riccardi, A. Smolyanitsky, Highly mechanosensitive ion channels from graphene-embedded crown ethers. *Nat. Mater.* **18**, 76–81 (2019).
22. S. Sahu, J. Elenewski, C. Rohmann, M. Zwolak, Optimal transport and colossal ionic mechano-conductance in graphene crown ethers. *Sci. Adv.* **5**, eaaw5478 (2019).
23. C. Kung, A possible unifying principle for mechanosensation. *Nature* **436**, 647–654 (2005).
24. H. Malmir, R. Epsztein, M. Elimelech, A. Haji-Akbari, Induced charge anisotropy: A hidden variable affecting ion transport through membranes. *Matter* **2**, 735–750 (2020).
25. J. Feng, K. Liu, M. Graf, M. Lihter, R. D. Bulushev, D. Dumcenco, D. T. L. Alexander, D. Krasnozhon, T. Vuletic, A. Kis, A. Radenovic, Electrochemical reaction in single layer MoS_2: Nanopores opened atom by atom. *Nano Lett.* **15**, 3431–3438 (2015).
26. M. Graf, M. Lihter, M. Thakur, V. Georgiou, J. Topolancik, B. R. Ilic, K. Liu, J. Feng, Y. Astier, A. Radenovic, Fabrication and practical applications of molybdenum disulfide nanopores. *Nat. Protoc.* **14**, 1130–1168 (2019).
27. H. Van Ngoc, Y. Qian, S. K. Han, D. J. Kang, PMMA-etching-free transfer of wafer-scale chemical vapor deposition two-dimensional atomic crystal by a water soluble polyvinyl alcohol polymer method. *Sci. Rep.* **6**, 33096 (2016).
28. L. Bocquet, E. Charlaix, Nanofluidics, from bulk to interfaces. *Chem. Soc. Rev.* **39**, 1073–1095 (2010).
29. K. Liu, T. Ding, X. Mo, Q. Chen, P. Yang, J. Li, W. Xie, Y. Zhou, J. Zhou, Flexible microfluidics nanogenerator based on the electrokinetic conversion. *Nano Energy* **30**, 684–690 (2016).
30. F. H. J. van der Heyden, D. Stein, C. Dekker, Streaming currents in a single nanofluidic channel. *Phys. Rev. Lett.* **95**, 116104 (2005).
31. P. B. Peters, R. van Roij, M. Z. Bazant, P. M. Biesheuvel, Analysis of electrolyte transport through charged nanopores. *Phys. Rev. E* **93**, 053108 (2016).

32. R. C. Rollings, A. T. Kuan, J. A. Golovchenko, Ion selectivity of graphene nanopores. *Nat. Commun.* **7**, 11408 (2016).
33. D. Stein, M. Kruithof, C. Dekker, Surface-charge-governed ion transport in nanofluidic channels. *Phys. Rev. Lett.* **93**, 035901 (2004).
34. M. R. Powell, L. Cleary, M. Davenport, K. J. Shea, Z. S. Siwy, Electric-field-induced wetting and dewetting in single hydrophobic nanopores. *Nat. Nanotechnol.* **6**, 798–802 (2011).
35. S. N. Smirnov, I. V. Vlassiouk, N. V. Lavrik, Voltage-gated hydrophobic nanopores. *ACS Nano* **5**, 7453–7461 (2011).
36. C. Lee, X. Wei, J. W. Kysar, J. Hone, Measurement of the elastic properties and intrinsic strength of monolayer graphene. *Science* **321**, 385–388 (2008).
37. S. Sahu, M. Zwolak, Golden aspect ratio for ion transport simulation in nanopores. *Phys. Rev. E* **98**, 012404 (2018).
38. S. Sahu, M. Zwolak, Maxwell-Hall access resistance in graphene nanopores. *Phys. Chem. Chem. Phys.* **20**, 4646–4651 (2018).
39. A. T. Celebi, C. T. Nguyen, R. Hartkamp, A. Beskok, The role of water models on the prediction of slip length of water in graphene nanochannels. *J. Chem. Phys.* **151**, 174705 (2019).
40. E. Wagemann, E. Oyarzua, J. H. Walther, H. A. Zambrano, Slip divergence of water flow in graphene nanochannels: The role of chirality. *Phys. Chem. Chem. Phys.* **19**, 8646–8652 (2017).
41. G. Tocci, L. Joly, A. Michaelides, Friction of water on graphene and hexagonal boron nitride from *ab initio* methods: Very different slippage despite very similar interface structures. *Nano Lett.* **14**, 6872–6877 (2014).
42. L. Gao, W. Ren, H. Xu, L. Jin, Z. Wang, T. Ma, L.-P. Ma, Z. Zhang, Q. Fu, L.-M. Peng, X. Bao, H.-M. Cheng, Repeated growth and bubbling transfer of graphene with millimetre-size single-crystal grains using platinum. *Nat. Commun.* **3**, 699 (2012).
43. A. Reina, H. Son, L. Jiao, B. Fan, M. S. Dresselhaus, Z. Liu, J. Kong, Transferring and identification of single- and few-layer graphene on arbitrary substrates. *J. Phys. Chem. C* **112**, 17741–17744 (2008).
44. W. H. Lee, J. Park, S. H. Sim, S. Lim, K. S. Kim, B. H. Hong, K. Cho, Surface-directed molecular assembly of pentacene on monolayer graphene for high-performance organic transistors. *J. Am. Chem. Soc.* **133**, 4447–4454 (2011).
45. S. Garaj, W. Hubbard, A. Reina, J. Kong, D. Branton, J. A. Golovchenko, Graphene as a subnanometre trans-electrode membrane. *Nature* **467**, 190–193 (2010).
46. H. J. C. Berendsen, J. R. Grigera, T. P. Straatsma, The missing term in effective pair potentials. *J. Phys. Chem. A* **91**, 6269–6271 (1987).
47. L. Lindsay, D. A. Broido, Optimized Tersoff and Brenner empirical potential parameters for lattice dynamics and phonon thermal transport in carbon nanotubes and graphene. *Phys. Rev. B* **81**, 205441 (2010).
48. I. S. Joung, T. E. Cheatham III, Determination of alkali and halide monovalent ion parameters for use in explicitly solvated biomolecular simulations. *J. Phys. Chem. B* **112**, 9020–9041 (2008).
49. Y. Wu, N. R. Aluru, Graphitic carbon–water nonbonded interaction parameters. *J. Phys. Chem. B* **117**, 8802–8813 (2013).
50. J. Gumbart, F. Khalili-Araghi, M. Sotomayor, B. Roux, Constant electric field simulations of the membrane potential illustrated with simple systems. *Biochim. Biophys. Acta* **1818**, 294–302 (2012).
51. J.-P. Ryckaert, G. Ciccotti, H. J. C. Berendsen, Numerical integration of the cartesian equations of motion of a system with constraints: Molecular dynamics of n-alkanes. *J. Comput. Phys.* **23**, 327–341 (1977).
52. W. M. Brown, P. Wang, S. J. Plimpton, A. N. Tharrington, Implementing molecular dynamics on hybrid high performance computers–short range forces. *Comput. Phys. Commun.* **182**, 898–911 (2011).
53. S. Plimpton, Fast parallel algorithms for short-range molecular dynamics. *J. Comput. Phys.* **117**, 1–19 (1995).
54. M. Mao, S. Ghosal, G. Hu, Hydrodynamic flow in the vicinity of a nanopore induced by an applied voltage. *Nanotechnology* **24**, 245202 (2013).
55. M. Heiranian, A. Taqieddin, N. R. Aluru, Revisiting Sampson's theory for hydrodynamic transport in ultrathin nanopores. *Phys. Rev. Res.* **2**, 043153 (2020).
56. E. J. G. Santos, E. Kaxiras, Electric-field dependence of the effective dielectric constant in graphene. *Nano Lett.* **13**, 898–902 (2013).
57. J. E. Hall, Access resistance of a small circular pore. *J. Gen. Physiol.* **66**, 531–532 (1975).
58. Y. Noh, N. R. Aluru, Ion transport in electrically imperfect nanopores. *ACS Nano* **14**, 10518–10526 (2020).
59. R. M. M. Smeets, U. F. Keyser, M. Y. Wu, N. H. Dekker, C. Dekker, Nanobubbles in solid-state nanopores. *Phys. Rev. Lett.* **97**, 088101 (2006).
60. C. P. Green, H. Lioe, J. P. Cleveland, R. Proksch, P. Mulvaney, J. E. Sader, Normal and torsional spring constants of atomic force microscope cantilevers. *Rev. Sci. Instrum.* **75**, 1988–1996 (2004).
61. R. J. T. Nicholl, H. J. Conley, N. V. Lavrik, I. Vlassiouk, Y. S. Puzyrev, V. P. Sreenivas, S. T. Pantelides, K. I. Bolotin, The effect of intrinsic crumpling on the mechanics of free-standing graphene. *Nat. Commun.* **6**, 8789 (2015).
62. J. C. Meyer, A. K. Geim, M. I. Katsnelson, K. S. Novoselov, T. J. Booth, S. Roth, The structure of suspended graphene sheets. *Nature* **446**, 60–63 (2007).
63. C. Lee, L. Joly, A. Siria, A.-L. Biance, R. Fulcrand, L. Bocquet, Large apparent electric size of solid-state nanopores due to spatially extended surface conduction. *Nano Lett.* **12**, 4037–4044 (2012).
64. M. Graf, M. Lihter, D. Unuchek, A. Sarathy, J.-P. Leburton, A. Kis, A. Radenovic, Light-enhanced blue energy generation using MoS_2 nanopores. *Joule* **3**, 1549–1564 (2019).
65. J. J. Vlassak, W. D. Nix, A new bulge test technique for the determination of Young's modulus and Poisson's ratio of thin films. *J. Mater. Res.* **7**, 3242–3249 (1992).
66. O. L. Blakslee, D. G. Proctor, E. J. Seldin, G. B. Spence, T. Weng, Elastic constants of compression-annealed pyrolytic graphite. *J. Appl. Phys.* **41**, 3373–3382 (1970).
67. Z. Dagan, S. Weinbaum, R. Pfeffer, An infinite-series solution for the creeping motion through an orifice of finite length. *J. Fluid Mech.* **115**, 505–523 (1982).
68. M. Heiranian, N. R. Aluru, Nanofluidic transport theory with enhancement factors approaching one. *ACS Nano* **14**, 272–281 (2020).
69. A. Berthod, J. J. Kozak, J. L. Anderson, J. Ding, D. W. Armstrong, Ionic liquid-alkane association in dilute solutions. *Theor. Chem. Acc.* **117**, 127–135 (2007).
70. E. Nightingale Jr., Phenomenological theory of ion solvation. Effective radii of hydrated ions. *J. Phys. Chem. A* **63**, 1381–1387 (1959).
71. M. E. Suk, N. R. Aluru, Ion transport in sub-5-nm graphene nanopores. *J. Chem. Phys.* **140**, 084707 (2014).

Acknowledgments: We thank X. Ding at the Center of Analytical Service at Zhejiang University for training TEM, W. Wang at the State Key Laboratory of Modern Optical Instrumentation for training FIB, and the Electron Microscopy Center and the Micro and Nano Fabrication Center at Zhejiang University for facility support. **Funding:** This study was funded by the National Natural Science Foundation of China (21974123), the National Key R&D Program of China (2020YFA0211200), the Natural Science Foundation of Zhejiang Province (LR20B050002), the Fundamental Research Funds for the Central Universities (2019XZZX003-01), and the Hundreds Program of Zhejiang University. Y.N. and N.R.A. were supported by the U.S. National Science Foundation (NSF) under grant nos. 1545907, 1708852, 1720633, and 1921578. The computing power was provided by the Extreme Science and Engineering Discovery Environment (XSEDE) granted by NSF with grant no. OCI-1053575 and Blue Waters supercomputing center, awarded by the state of Illinois and NSF, OCI-0725070 and ACI-1238993. **Author contributions:** X.J. and C.Z. fabricated the devices and performed the measurements and data analysis. C.Z. performed graphene growth and TEM imaging. Y.N. performed the computational studies and developed the analytical model under the guidance of N.R.A. Y.X. conducted atomic force microscopy analysis. Y.C. analyzed the data. F.C. fabricated the substrates. L.M. and W.R. provided high-quality graphene samples. J.F. conceived and supervised the project. J.F., Y.N., X.J., and N.R.A. cowrote the paper. All authors contributed to the general discussions. **Competing interests:** The authors declare that they have no competing interests. **Data and materials availability:** All data needed to evaluate the conclusions in the paper are present in the paper and/or the Supplementary Materials.

Submitted 29 April 2021
Accepted 22 November 2021
Published 14 January 2022
10.1126/sciadv.abj2510

ScienceAdvances

Nonlinear electrohydrodynamic ion transport in graphene nanopores

Xiaowei JiangChunxiao ZhaoYechan NohYang XuYuang ChenFanfan ChenLaipeng MaWencai RenNarayana R. AluruJiandong Feng

Sci. Adv., 8 (2), eabj2510. • DOI: 10.1126/sciadv.abj2510